

Competitive kinetic model for the pyrolysis of the Phenolic Impregnated Carbon Ablator

Torres Herrador, Francisco José; Coheur, Joffrey; Panerai, Francesco; Magin, Thierry; Arnst, Maarten; Mansour, Nagi N; Blondeau, Julien

Published in:
Aerospace Science and Technology

DOI:
[10.1016/j.ast.2020.105784](https://doi.org/10.1016/j.ast.2020.105784)

Publication date:
2020

License:
CC BY-NC-ND

Document Version:
Accepted author manuscript

[Link to publication](#)

Citation for published version (APA):

Torres Herrador, F. J., Coheur, J., Panerai, F., Magin, T., Arnst, M., Mansour, N. N., & Blondeau, J. (2020). Competitive kinetic model for the pyrolysis of the Phenolic Impregnated Carbon Ablator. *Aerospace Science and Technology*, 100, [105784]. <https://doi.org/10.1016/j.ast.2020.105784>

Copyright

No part of this publication may be reproduced or transmitted in any form, without the prior written permission of the author(s) or other rights holders to whom publication rights have been transferred, unless permitted by a license attached to the publication (a Creative Commons license or other), or unless exceptions to copyright law apply.

Take down policy

If you believe that this document infringes your copyright or other rights, please contact openaccess@vub.be, with details of the nature of the infringement. We will investigate the claim and if justified, we will take the appropriate steps.

Competitive kinetic model for the pyrolysis of the Phenolic Impregnated Carbon Ablator

Francisco Torres-Herrador^{a,b,*}, Joffrey Coheur^{a,c}, Francesco Panerai^d, Thierry E. Magin^a, Maarten Arnst^c, Nagi N. Mansour^e, Julien Blondeau^b

^a*von Karman Institute for Fluid Dynamics, 1640 Rhode-St-Genese, Belgium*

^b*Thermo and Fluid dynamics (FLOW), Faculty of Engineering, Vrije Universiteit Brussel (VUB), 1050 Brussels, Belgium*

^c*Université de Liège, Aerospace and Mechanical Engineering, Allée de la Découverte 9, 4000 Liège, Belgium*

^d*University of Illinois at Urbana-Champaign, Urbana, IL 61801, USA*

^e*NASA Ames Research Center, CA 94035 Moffett Field, USA*

Abstract

Carbon/phenolic ablators are successfully used as thermal protection material for spacecraft. Nevertheless, their complex thermal degradation is not yet fully understood, and current pyrolysis models do not reproduce important features of available experimental results. Accurate and robust thermal degradation models are required to optimize design margin policy. We investigate whether the competitive kinetic schemes commonly used to model biomass pyrolysis are appropriate to describe the thermal degradation of carbon/phenolic composites. In this paper, a competitive pyrolysis model for the thermal degradation of the carbon/phenolic ablator PICA is proposed. Model parameters are then calibrated using a robust two-step methodology: first deterministic optimization is used to obtain the best estimation of the calibration parameters based on the experimental data, then a stochastic

*Corresponding author. fratorhe@vki.ac.be (F. Torres-Herrador)

Bayesian inference is performed to explore plausible set of solutions taking into account the experimental uncertainties. The calibrated model provides an accurate description of the pyrolysis process at different heating rates. The model shows great flexibility and robustness at a similar computational cost as the traditional devolatilization models. This opens the possibility for more complex mechanisms when more experimental data becomes available.

Keywords: Carbon/phenolic composite, Kinetics, pyrolysis, optimization

Nomenclature

Acronyms

CV Coefficient of Variation

DTGA Differential TGA

GA Genetic Algorithm

MCMC Markov Chain Monte Carlo

MSL Mars Science Laboratory

PDF Probability Distribution Function

PICA Phenolic Impregnated Carbon Ablator

RWMH Random Walk Metropolis Hastings

SCE Shuffled Complex Evolution

TACOT Theoretical Ablative Composite for Open Testing

TGA Thermogravimetric Analysis

TPS Thermal Protection System

Greek Symbols

η Numerical model

γ Stoichiometric coefficient

[−]

π Probability density function

Σ Covariance Matrix

τ Weighting factor

ε Observation error

Indexes

0 Initial condition

∞ Final conditions

amb Ambient conditions

| | | | |
|----------------------|---|----------|--|
| obs | Observed | A | Matrix of reaction rates |
| P | Product | d | Data set |
| r | Reactant | p | Calibration parameter set |
| sim | Simulated | W | Weighting operator |
| Roman Symbols | | | |
| \mathcal{A} | Pre-exponential factor $[\text{s}^{-1}]$ | J | Proposal distribution |
| \mathcal{E} | Activation energy $[\text{J mol}^{-1}]$ | k | Reaction rate $[\text{s}^{-1}]$ |
| \mathcal{G} | Gas | m | Order of reaction $[-]$ |
| \mathcal{P}_{ad} | Set of admissible solutions | n_p | Number of competitive branches from a given component |
| \mathcal{R} | Universal gas constant $[\text{J K}^{-1} \text{mol}^{-1}]$ | r | Acceptance ratio |
| \mathcal{S} | Solid | S | Objective function |

1. Introduction

Pyrolysis of phenol-formaldehyde resins is extensively studied due to ubiquitous use of the resins in industrial processes, and manufacturing of composite materials. A niche application is in the use of these resins in thermal protection materials. An example application is their use in composites materials in spacecraft heatshields. During atmospheric entry at hypersonic speeds, most of the kinetic energy due to drag deceleration is transformed into thermal energy, resulting in substantial heat transferred to the spacecraft. Extreme temperatures reached at the surface require an efficient Thermal Protection System (TPS) to insulate the spacecraft and protect the payload. For systems that need superior insulation capabilities

and low mass, lightweight carbon/phenolic ablators are preferred material architecture. This class of ablators consists of composite materials made of carbon fibers bound together into rigid or flexible preforms [1] and infused with a high surface area phenolic resin phase [2]. A notable example within this class is the Phenolic Impregnated Carbon Ablator (PICA) developed by NASA which has been successfully used in missions such as Mars Science Laboratory (MSL) [3] or Stardust Sample Return Capsule [4]. The high porosity and surface area of the composite results in low conductivity that retards the heat fluxes towards the interior of the material, ensuring thermal insulation of the vehicle. In addition, the phenolic resin decomposes via globally endothermic pyrolysis resulting in flux of pyrolysis gases [5] blown into the boundary layer that partially block the incoming heat. Understanding the process of pyrolysis is fundamental to improve physical models that are used in numerical simulations of thermal protection systems response to high-enthalpy environments.

Thermal degradation via pyrolysis involves a series of complex chemical interactions [6]. In these processes, the long polymeric chains of the solid phenolic break up with the consequent release of gases and leading to a carbonaceous char. In ablator response models for PICA, pyrolysis has been traditionally modeled assuming the presence of several solid phases of density ρ_i that decompose following a set of independent parallel reactions [7–12]. Arrhenius-type reactions are used and reaction constants are calibrated based on experimental measurements of mass loss versus temperature from thermogravimetric analysis (TGA) [13]. In rare instances calibration accounts for species or elemental production measured with gas sampling techniques

[12]. This approach that assumes independent reactions is strictly valid for a given (and usually narrow) range of heating rate conditions for which the model was calibrated. However, it lacks in generality and fails when applied to largely different heating rates. For ablation modeling at varying heating rates this is a substantial limitation, no longer acceptable as we aim at physics-based predictions of the ablation phenomenon [14]. Indeed, a broad range of heating rates is found in ablative heat shields used in atmospheric entry. Consider the case of MSL as an example [15]: heating rates vary dramatically in space across the heat shield, both span-wise and in-depth, and in time at different phases of an entry trajectory. Values as high as $60\,000\text{ K min}^{-1}$ and as low as 60 K min^{-1} can be found. In addition, most of flight heating rates are outside the realm of legacy TGA measurements used for calibration, rarely exceeding tens of K min^{-1} .

In solid-phase pyrolysis, it is usually observed that as the heating rate increases, the decomposition curves shift towards higher temperatures [12]. This behavior is commonly attributed to the thermal lag effects and can be usually reproduced assuming independent parallel reactions. However, different experimental evidences [16, 17] show that this is not the case for the pyrolysis of carbon/phenolic. For example, Stokes [17] observed that at heating rates higher than 300 K min^{-1} the pyrolysis peak shifted towards lower temperatures. The same effect was also observed in recent pyrolysis experiments from Wong et al. [18] and Bessire and Minton [19], further discussed in Sect. 4. This shift towards lower temperatures suggests that several reactions consuming the same reactant are occurring simultaneously, or in other words, that two (or more) reactions are in competition. Legacy pyrolysis mechanisms

do not account for such behavior because of their parallel and independent reaction formulation [8–12]. Effects of competitive reactions are not only observed in the degradation of carbon/phenolic composites, but also in the pyrolysis of biomass materials [20]. In order to model the devolatilisation of various biomass feedstocks, many competitive reaction mechanisms have been developed which are capable of assessing these variations for different wood species as well as different levels of detail [21–23].

Given the differences in the pyrolysis models found in aerospace engineering literature, the lack of generality of the existing models to reproduce different experimental observations, this work intends to: (1) propose a generalized pyrolysis scheme by including competitive mechanisms to the classical parallel reactions used for modeling the thermal degradation of carbon/phenolic material, (2) provide a robust methodology for parameter calibration based on experimental data, and finally, (3) present a reaction scheme based on the two first items for the decomposition of PICA based on modern experimental data [18, 19].

This paper is organized as follows. Firstly, we generically describe the thermal degradation of a solid under the hypothesis of competitive reactions in Sect. 2.1. We then establish a general notation for multicomponent competitive mechanisms, highlighting the link between this general modeling with the classical independent parallel reactions used for TPS as a particular case. Secondly, in Sect. 3, the methodology for the calibration in a deterministic and a probabilistic framework is described and, in Sect. 4 the experimental datasets used in this work are presented. Following, we propose a competitive mechanism which phenomenologically can describe

the experimental observations in Section Sect. 5. Then, the kinetic rates constants are calibrated using both the deterministic and the probabilistic optimization framework. Finally, the resulting scheme is evaluated at a broad range of heating rates in order to assess its performance and compared with other experimental data from Bessire and Minton [19] to assess extrapolation capabilities of the model.

2. Pyrolysis Model

2.1. Simple competitive kinetics scheme

A competitive kinetic model can be represented as a branching tree. An initial solid reactant may react producing pyrolysis gases and other solid products. These products, in turn, may become reactants thus following a branched process. Let us consider a solid reactant of density ρ^r that generates n^p products as sketched in Fig. 1. These reactions can either refer to elementary processes or to global reactions. While elementary processes describe in detail the decomposition of each molecule, in a global approach the chemistry is encapsulated in phenomenologically coherent steps. Elementary processes are more accurate but they are difficult to resolve with current experimental methods. Therefore, global reaction schemes are the most common approach in pyrolysis modeling [22]. In addition, global reactions reduce the number of calculations which enables these schemes to be conveniently integrated in material degradation codes.

The evolution of each reaction i is controlled by its kinetic rate k_i . In the present case, kinetic rates are modeled using a first order Arrhenius equation

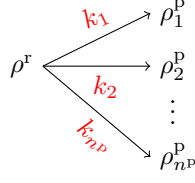


Figure 1: Illustration of a competitive mechanism. A solid ρ^r reacts producing n^p products.

of the form

$$k_i = \mathcal{A}_i \exp(-\mathcal{E}_i/\mathcal{R}T), \quad (1)$$

where \mathcal{R} is the universal gas constant, \mathcal{A}_i is the pre-exponential factor, and \mathcal{E}_i is the activation energy for the i -th reaction. The solid reactant will degrade generating product, ρ_i^p at a rate given by

$$\frac{d\rho_i^p}{dt} = k_i(\rho^r)^{m_i}, \quad (2)$$

where the exponent m_i (sometimes referred to as the reaction order) is often set to 1 in pyrolysis applications [24] and will be omitted in the following analysis for simplicity and clarity.

Now, considering n_p simultaneous reactions that the solid reactant may undergo, the total decomposition rate of the solid can be expressed as

$$\frac{d\rho^r}{dt} = -\sum_{i=0}^{n^p} \frac{d\rho_i^p}{dt} = -\sum_{i=0}^{n^p} k_i \rho^r. \quad (3)$$

2.2. Generalized competitive kinetics model

Generalized pyrolysis scheme of multicomponent competitive reaction mechanisms is represented in Fig. 2. Let A_i be all the species expected in the system of reactions, $i = 1, \dots, n$, which can be either a gaseous species $i \in I_G$ or solid species (reactant or product) $i \in I_S$, thus $i \in I_S \cup I_G$ are all of the species that are in the system considered. The number of species in each

set is $|I_G| = n_G$ and $|I_S| = n_S$ respectively with the total number of species $n = n_G + n_S$. The density of the solid phase is then expressed as,

$$\rho_S = \sum_{i=1}^{n_S} \epsilon_i \rho_i \quad (4)$$

where ϵ_i is the volume fraction of solid species.

Competitive mechanisms occur on the i -th component with density ρ_i following the reaction rate $k_{i,j}$ where j is the index for its j -th competitive branch. The number of competitive reactions for the component ρ_i (Fig. 2) is n_i^p . Each reaction may generate more than one product species, A_l from either, I_S or I_G ,

$$p_{i,j,l} \rightarrow \sum_{l=1}^n \zeta_{i,j,l} A_l, \quad \forall i \in [1, n] \quad (5)$$

where $\zeta_{i,j,k}$ are the stoichiometric coefficients. Thus mass coefficients $\gamma_{i,j,l}$ are introduced,

$$\gamma_{i,j,k} = \frac{\zeta_{i,j,k}}{\sum_{j=1}^{n_i^p} \sum_{l=1}^n \zeta_{i,j,l} \rho_l}. \quad (6)$$

We have from stoichiometry and mass conservation

$$\gamma_{i,j,k} = 0, \quad \forall i = k, \forall j \in n_i^p. \quad (7)$$

For $i \in I_S$, the variation of a component ρ_i is given by the balance between the production and destruction of component ρ_i as

$$\frac{d\rho_i}{dt} = - \underbrace{\sum_{j=1}^{n_i^p} k_{i,j} \rho_i}_{\text{destruction of } \rho_i} + \underbrace{\sum_{j=1}^n \sum_{l=1}^{n_j^p} k_{j,l} \gamma_{j,l,i} \rho_j}_{\text{production of } \rho_i}. \quad (8)$$

The first term on the right-hand side (RHS) is the destruction of ρ_i , which is the sum over all reaction branches from the solid component ρ_i towards products. This term is zero for gases since it is assumed that only solid

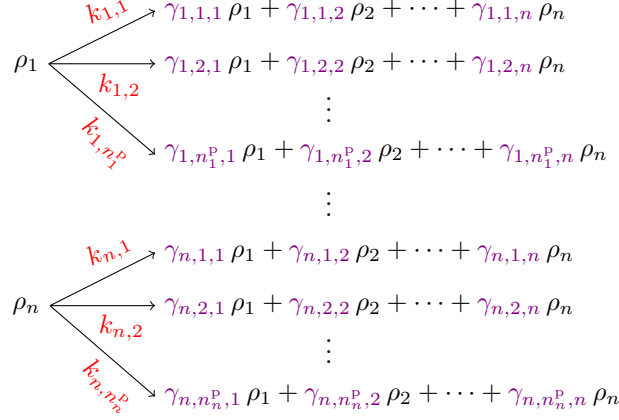


Figure 2: Generalized pyrolysis scheme of a multicomponent competitive mechanisms.

components pyrolyze while gas phase reactions will be computed elsewhere, thus $k_{i,j} = 0$ for $i \in I_G$. The second term represents the production term of component ρ_i coming from all other components (except from $j = i$ for which this term is zero from Eq. 7) arrows pointing towards the components ρ_i , from which we sum over all reaction component and all parallel branches.

Eq. 8 defines a system of first order Ordinary Differential Equations (ODEs) that can be written under a matrix formalism as

$$\frac{d\boldsymbol{\rho}}{dt} = \mathbf{A}\boldsymbol{\rho}, \quad (9)$$

where $\boldsymbol{\rho}$ is a column vector with all the components ρ_i and \mathbf{A} is the matrix of coefficients. Diagonal terms of \mathbf{A} , a_{ii} , are given by the first term on the RHS of Eq. 8 while off-diagonal terms by the second term (note that $\gamma_{j,l,i} = 0$ for $j = i$, i.e. no self-production term). This system is linear and the coefficients will be generally non-constant due to the temperature dependence of the reaction rates, rendering the solution hard to obtain analytically. When the coefficient matrix \mathbf{A} is constant (isothermal pyrolysis) the matrix-exponential method

can be used. For a non-constant coefficient matrix \mathbf{A} , as in multi-component reactions, the ordinary differential equation system, Eq. 9, will have to be integrated numerically. \mathbf{A} is of full rank if all the dependent variables are removed, which are all the gaseous products and solid products that do not further react. Once this is removed from the system of equations, it can be shown that \mathbf{A} can be written under the form of a lower triangular matrix if no backward reactions are considered [24]. Such backward loops are not observed in practice for pyrolysis reactions because they are highly dissipative and irreversible. The system of equations can be easily solved using the Gauss-Jordan method, as the matrix is already triangular.

In addition, it can be shown that the generalized model degenerates in a parallel model if the second term on the RHS (Eq. 8) is 0 [25], in that case, the system becomes a diagonal matrix and analytical solutions can be found [25].

Generating different products from the same reactant provides great flexibility to the competitive reaction mechanisms. This means that different kinetic pathways may become dominant depending on the heating conditions leading to the possibility of “selecting” the pathway. This is intensively used in biomass pyrolysis where this selectivity allows to predict which products (gas, char or tar) will be mostly produced [20].

Due to the nature of competitive schemes, a component ρ_i can be produced and consumed during the pyrolysis process (non diagonal matrix \mathbf{A}). This makes that the advancement of reaction becomes irrelevant to describe the evolution of a particular reaction. A workaround to this is to describe the state of the reaction in terms of densities and if required define a global

advancement of reaction from virgin to char [24, 26].

3. Model calibration and uncertainty quantification

Calibration of kinetic models is usually performed in a deterministic framework using optimization algorithms to achieve fits to experimental data [12, 26]. In addition, we intend here to provide a calibrated model that takes into account the experimental uncertainties for a more robust characterization of model parameters using methods from statistics and Bayesian inference. Literature on Bayesian inference for chemical kinetics is scarce and most of it is on homogeneous reactions in a mixture for combustion applications [27–30]. For pyrolysis applications, one can cite the work of Bruns [31] who applied Bayesian inference on dependent non-competitive pyrolysis reactions for high-impact polystyrene, bisphenol-A polycarbonate and polyvinyl chloride based on TGA data at two different heating rates (3 and 10 K min⁻¹) relevant to fire applications.

In the following, we describe a two-step methodology for parameter calibration based first on a deterministic approach and then a probabilistic (Bayesian) approach. A robust methodology which ensures a global optimum is particularly important for competitive mechanisms due to the large parameter space and the possibility of getting trapped in a local minimum [24, 26].

The relationship between the observed data d_k^{obs} and the computer model $\eta(\cdot, \cdot)$, here the pyrolysis model, is represented as

$$d_k^{\text{obs}} = \eta(\mathbf{x}_k, \mathbf{p}) + \varepsilon_k, \quad (10)$$

where ε_k is the observation error for the k -th observation among the n_{obs} observations (model structure error not considered here). The computer model

η is a function of two inputs: 1) the calibration parameters \mathbf{p} , which we wish to learn about or optimize and 2) the variable inputs \mathbf{x}_k whose values may change during the calibration process. For the pyrolysis decomposition model (Eqs. 1 and 8) the uncertain parameter set is the vector of the calibration parameters $\mathbf{p} = \{\mathcal{A}_{ij}, \mathcal{E}_{ij}, \gamma_{ijl}\}$. The variable inputs \mathbf{x}_k are, in this case, the time or temperature assumed to be known with certainty from experiments. In the following, we denote \mathbf{d}^{obs} as the vector of experimental observations d_k^{obs} .

In a deterministic inverse problem, one estimates a single value \mathbf{p}_0 for the parameters with a best fit approach. Conversely in Bayesian inference, the observation errors and the parameters \mathbf{p} are considered as random quantities and the result of the identification process is the so-called Bayesian posterior probability density $\pi(\mathbf{p}|\mathbf{d}^{\text{obs}})$ on the parameters given the observations [32, 33]). These two approaches are described in the following sections.

3.1. Deterministic inverse problem

In the following, we denote $\mathbf{d}(\mathbf{p}) = (\eta(\mathbf{x}_1, \mathbf{p}), \dots, \eta(\mathbf{x}_{n_{\text{obs}}}, \mathbf{p}))$ the vector of simulation results at different values of \mathbf{x}_k for the parameters \mathbf{p} , \mathbf{W} a weighting matrix and use the concept of weighted norms defined as

$$\frac{1}{2} \|\mathbf{d}(\mathbf{p}) - \mathbf{d}^{\text{obs}}\|_{\mathbf{W}}^2 = \frac{1}{2} (\mathbf{d}(\mathbf{p}) - \mathbf{d}^{\text{obs}})^{\top} \mathbf{W} (\mathbf{d}(\mathbf{p}) - \mathbf{d}^{\text{obs}}), \quad (11)$$

where $\|\cdot\|_{\mathbf{W}}$ denotes the weighted norm. In the deterministic inverse problem, one generally minimizes a measure of the mismatch, or objective function, $S(\mathbf{p})$ between the computer model outputs and the observed data. Considering the norm as a measure of this mismatch, we have

$$S(\mathbf{p}) = \frac{1}{2} \|\mathbf{d}(\mathbf{p}) - \mathbf{d}^{\text{obs}}\|_{\mathbf{W}}^2. \quad (12)$$

The deterministic inverse problem consists then in finding the best solution that minimizes this misfit function

$$\mathbf{p}_0 = \arg \min_{\mathbf{p} \in \mathcal{P}_{\text{ad}}} 2S(\mathbf{p}), \quad (13)$$

where \mathcal{P}_{ad} is the set of admissible solutions and \mathbf{p}_0 is the best estimate for which the model fits the observed data best. In the case of the misfit stated in Eq. 12, and considering the weighting matrix to be the identity matrix, the optimization problem in Eq. 13 is the standard least-squares problem.

Because of nonlinearities induced by the kinetic rates, the objective function may not necessarily be convex in this case. This means that multiple local minima can provide satisfactory combinations of kinetic parameters [26]. Therefore, gradient-based optimization algorithms may get “trapped” in one of these local minima. In addition, traditional Genetic Algorithms (GA) have proven to be slow when applied in large search spaces and less precise [26].

Considering this, the optimization method chosen in this work is the “Shuffled Complex Evolutionary Algorithm” (SCE) included in the optimization package SPOTPY [34]. This optimization method, proposed by Duan et al. [35] performs an optimization at two levels: a global and a local search. Similarly to a GA, an initial population of individuals is randomly generated from admissible set of solutions or search space. For each parameter $p_i \in \mathbf{p}$ this search space is defined as $p_i \in [p_i^{\min}, p_i^{\max}] = \{p_i \in \mathbb{R} \mid p_i^{\min} \leq p_i \leq p_i^{\max}\}$. An individual refers to a realization of the parameter set \mathbf{p} . At each iteration of the algorithm, the population is grouped into a user-defined number of local search groups. A local search is performed within these groups, using a swarm-like optimization [35]. Once this process is finished for the different groups, the individuals are shuffled (hence the name of the method) such

that the most promising individuals will have higher chances of continuing the optimization process, thus exchanging information about the search space in a similar way to traditional GA. An individual is evaluated through comparison with the experimental data (Eq. 12). Here, for each experimental measurement, a simulation of the pyrolysis is carried out using the proposed mechanism with a realization of the parameter set \mathbf{p} . Then, this result is compared to the experiments providing a measure of the fitness of the individual similarly to Eq. 12. Two observation sets from the experiments that contribute to the objective function S that are the TGA data and its derivative (DTGA) [26]. While the TGA curve provides the general shape of the curve, its derivative accurately captures the maxima of the production rates and a weighting factor $\tau = 10000$ is set to scale the two contributions up to the same order of magnitude, leading to the final vector of simulation results, vector of observations and weighted operator

$$\mathbf{d}(\mathbf{p}) = \mathbf{d}^{\text{sim}} = (\mathbf{d}_{\text{TGA}}^{\text{sim}} \ \mathbf{d}_{\text{DTGA}}^{\text{sim}}), \quad (14)$$

$$\mathbf{d}^{\text{obs}} = (\mathbf{d}_{\text{TGA}}^{\text{obs}} \ \mathbf{d}_{\text{DTGA}}^{\text{obs}}), \quad (15)$$

$$\mathbf{W} = \begin{pmatrix} \mathbf{I}_{n_{\text{obs}}/2} & \mathbf{0} \\ \mathbf{0} & \tau \mathbf{I}_{n_{\text{DTGA}}^{\text{obs}}} \end{pmatrix}, \quad (16)$$

which is equivalent to the following objective function

$$S = \|\mathbf{d}_{\text{TGA}}^{\text{sim}} - \mathbf{d}_{\text{TGA}}^{\text{obs}}\|_{\mathbf{I}_{n_{\text{obs}}/2}}^2 + \tau \|\mathbf{d}_{\text{DTGA}}^{\text{sim}} - \mathbf{d}_{\text{DTGA}}^{\text{obs}}\|_{\mathbf{I}_{n_{\text{DTGA}}^{\text{obs}}}}^2, \quad (17)$$

and where the superscripts “sim” and “obs” refer to the simulated and the experimental observations respectively.

In addition to its advantages regarding the efficient exploration of large search spaces, the SCE algorithm can be also considered trivially parallel since

the different local groups can run independently, thus reducing the overall computational time.

3.2. Stochastic inverse problem

The optimization process previously described provides a way to find the parameters \mathbf{p}_0 that best fit the observations \mathbf{d}^{obs} . However, this deterministic framework does not take into account the uncertainties on the observations that could lead to a different value of \mathbf{p}_0 . Although it is possible to use regularization techniques in the deterministic approach, the Bayesian probabilistic framework briefly described below provides a natural way of incorporating those uncertainties.

In Bayesian inference, the posterior probability density, namely the result of the identification process, is given by the Bayes' formula:

$$\pi(\mathbf{p}|\mathbf{d}^{\text{obs}}) = \frac{\pi(\mathbf{d}^{\text{obs}}|\mathbf{p})\pi_0(\mathbf{p})}{\int_{\mathfrak{R}^m} \pi(\mathbf{d}^{\text{obs}}|\mathbf{p})\pi_0(\mathbf{p})d\mathbf{p}}. \quad (18)$$

Here, $\pi_0(\mathbf{p})$ is the prior probability density and $\pi(\mathbf{d}^{\text{obs}}|\mathbf{p})$ is the likelihood function. The likelihood function evaluates the plausibility of a value \mathbf{p} of the parameters by calculating the density of probability of observing the data \mathbf{d}^{obs} given that value of the parameters. It is assumed the observation errors to be independent and identically distributed following a Gaussian density of known variance σ_k . The likelihood function provided the observations is given by

$$\pi(\mathbf{d}^{\text{obs}}|\mathbf{p}) = \frac{1}{(\prod_k \sigma_k)(2\pi)^{n^{\text{obs}}/2}} \exp\left(-\frac{1}{2}\|\mathbf{d}(\mathbf{p}) - \mathbf{d}^{\text{obs}}\|_{\mathbf{w}}^2\right) \quad (19)$$

and the weighting factor is given by

$$\mathbf{W} = \begin{pmatrix} \boldsymbol{\Sigma}_{\text{TGA}}^{-1} & \mathbf{0} \\ \mathbf{0} & \boldsymbol{\Sigma}_{\text{DTGA}}^{-1} \end{pmatrix}, \quad (20)$$

where the covariance matrices $\boldsymbol{\Sigma}_{\text{TGA}}$ and $\boldsymbol{\Sigma}_{\text{DTGA}}$ are diagonal matrices and are directly obtained from the experimental measurements as will be described in Sect. 4. The prior density should compile all the information about the parameters before taking into account the data. Because of the absence of prior knowledge about the distribution of the parameters, it is assumed a joint uniform prior distribution whose upper bounds are large enough so that the result of the inference is not influenced and lower bounds come from physical constraints (strictly positive), which results in the same expression as for the search space in the optimization method. The posterior density is what we know about the parameters after observing the data and it is the objective of the inference. In Bayesian inference, computations with Bayesian posteriors are performed by random explorations of the posterior distribution that provide samples directly drawn from it. These samples can then be used to estimate statistics of the posterior distribution (e.g. mean, variance, etc) using Monte Carlo integration, or for propagation through numerical solvers for uncertainty quantification.

Markov Chain Monte Carlo (MCMC) methods are a general class of sampling methods to draw samples from a target distribution, here the posterior distribution $\pi(\mathbf{p}|\mathbf{d}^{\text{obs}})$ [36]. A robust MCMC method is the Metropolis–Hastings algorithm, first proposed by Metropolis et al. [37] and later generalized by Hastings [38]. Starting from a value \mathbf{p}_0 , this algorithm draws samples from a distribution, J , thereon called proposal distribution,

that is easier to simulate. The proposed samples \mathbf{p}^* are then accepted or rejected according to an acceptance probability [33, 39]. The accepted samples \mathbf{p}_l characterize fully the posterior distribution.

In practice, we only need to sample from J for determining the new value of the estimate \mathbf{p}^* . Finally, when the proposal distribution is of the form $J(\mathbf{p}^*|\mathbf{p}_{l-1}) = J(|\mathbf{p}^* - \mathbf{p}_{l-1}|)$ such as a Gaussian distribution, then the algorithm is called Random Walk Metropolis-Hastings (RWMH). We choose the proposal distribution to be a multivariate Gaussian distribution centered on \mathbf{p}_{l-1} with covariance matrix Σ

$$J(\mathbf{p}^*|\mathbf{p}_{l-1}) = \frac{1}{\sqrt{(2\pi)^{n_{\mathbf{p}}}\det\Sigma}} \exp\left(-\frac{1}{2}(\mathbf{p}^* - \mathbf{p}_{l-1})^T \Sigma^{-1}(\mathbf{p}^* - \mathbf{p}_{l-1})\right). \quad (21)$$

The initial covariance matrix Σ will be assumed to be a diagonal matrix where the diagonal elements are tuned by trial-and-error to reach a good acceptance rate.

The starting value \mathbf{p}_0 of a MCMC chain can seriously deteriorate the convergence of the chain causing a large burn-in phase. This is especially true for multimodal likelihood functions as the chain can get trapped into a local minimum. The number of iterations it remains trapped will depend strongly on the goodness of approximation of the proposal function to the posterior distribution. To overcome this problem, the Markov chain is initialized with the best estimates \mathbf{p}_0 resulting from the global optimization search on the whole parameter space.

The overall Bayesian procedure is implemented within an in-house python package: PYthon Bayesian Inference Toolbox and Uncertainty Propagation (PYBITUP). This package includes standard MCMC methods such as the

RWMH used in this work. In Sect. 6.4, uncertainty propagation is performed to other heating rates using the results of the Markov chains obtained from the calibration using direct Monte Carlo simulations.

4. Description of experimental data

To calibrate the model for PICA we used two sets of data obtained from independent experimental efforts [18, 19]. While other data exist on the pyrolysis of the SC1008 phenolic system [40] and similar resins [41], the selected sets constitute the most modern data on the material. These experiments measured the actual aerogel formulation of PICA’s resin and covered a wide range heating rates.

The first data-set comes from Wong et al. [18], who performed traditional TGA measurements using a commercial TGA device (SEIKO SSC/5200 TG/DTA220). In this experiment, the mass loss of a 2.2mg sample of PICA was monitored during the temperature ramp at a low heating rate of 10 K min^{-1} . For convenience of the present analysis, the noise of the decomposition curve from [18] is smoothed using a Savitzky-Golay filter [42] and corrected for possible TGA buoyancy effects. This noise gives a measure of the variance on the mass loss appearing in Eqs. 19 and 20 which is approximately a linear function of temperature. About its derivative, it is not straightforward on how to obtain the experimental noise as the derivative of the signal depends mainly on the quality of the filter, which is itself noisy. Therefore, this quantity will not be used in the Bayesian inference.

The second data-set is from the experiments of Bessire and Minton at 366 K min^{-1} [19]. Their experiments consisted of a PICA sample which was

resistively heated by passing a high current through the carbon fiber preform substrate of PICA. Monitoring the temperature using a thermocouple located in the center of the material and using a control system, the authors were able to achieve heating rates much higher than those of traditional TGA systems. The pyrolysis products from the PICA sample were collected and analyzed with a time-of-flight mass spectrometer, which allowed to quantify 14 characteristic molecules from the pyrolysis of PICA. This included permanent gases, water and hydrocarbons (up to C_8). The authors measured the experimental variability by repeating three times their experiments. They expressed the results with a mean and a standard deviation. The global mean value is obtained by summing all the curves and the standard deviation is obtained by assuming Gaussian independent noises for each production curve. As a first approximation, we will use this variance in the likelihood function that we will further relax to account for additional variability. Finally, TGA-like mass loss versus temperature (or time) curves were reconstructed by integrating the measured gas production rates. Again, variance on reconstructed curves is not trivial to estimate due to numerical errors and we do not use this quantity in the Bayesian inference. However, estimated variance from resampling will be used to assess the accuracy of the extrapolated curves with uncertainties in Sect. 6.4.

It can be seen in Fig. 3 that the low heating rate data (in blue, Wong et al. [18]) is shifted towards substantially higher temperatures compared to the high heating rate data (orange, Bessire and Minton [19]). This effect has been reported in the literature [16, 17] for carbon/phenolic composites, but has never been considered in traditional kinetic models for PICA. Indeed, the

devolatilization mechanisms based on parallel reactions currently in use are not able to reproduce this effect due to their mathematical formulation as proven in previous work [25].

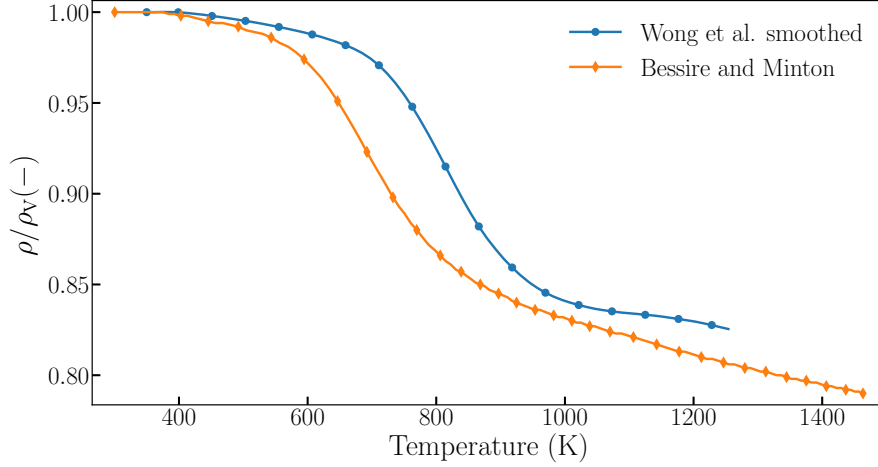


Figure 3: Experimental data used for model calibration. In blue, TGA (10 K min^{-1}) data from Wong et al.[18] filtered to reduce noise and buoyancy effect. In orange, the data from Bessire and Minton (366 K min^{-1}) [19].

5. Reaction scheme proposed for PICA

The proposed kinetic model needs to be coherent with the experimental data presented in Sect. 4. The observation that at high heating rates the decomposition curve shifts towards lower temperatures suggests the need to segregate the model into a “*low heating rate*” and a “*high heating rate*” pathway as depicted in Fig. 4.

In the following, the superscripts \mathcal{G} and \mathcal{S} are used to clarify which components are gaseous or solids respectively. In addition, the superscript “*”

highlights intermediate solids that are produced without release of pyrolysis gases in a depolymerization process [21]. The initial reactant ρ_1^S decomposes into two different branches: a slow $k_{1,1}$ process for low heating rates and a fast one $k_{1,2}$ for high heating rates. The slow branch progressively depletes the reactant starting at lower temperatures ($\mathcal{E}_{1,1} < \mathcal{E}_{1,2}$) and requires time to be completed. Therefore, at low heating rates, decomposition is dominated by such process and the intermediate solid $\rho_2^{S,*}$ is produced. At high heating rates, the fast process $k_{1,2}$ becomes active and dominant. This process decomposes most ρ_1^S , producing the intermediate $\rho_3^{S,*}$, while impeding the production of $\rho_2^{S,*}$. Each intermediate solid ($\rho_2^{S,*}$ and $\rho_3^{S,*}$) will further react at rates $k_{2,1}$ and $k_{3,1}$ into charred solids ρ_4^S and ρ_6^S , with the corresponding release of pyrolysis gases ρ_5^G and ρ_7^G , respectively.

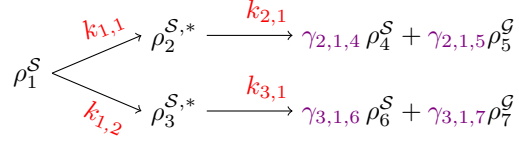


Figure 4: Proposed competitive mechanism for the thermal degradation of PICA.

The reaction scheme depicted in Fig. 4 can be written as ODEs' system

of the form shown in Eq. 9 as

$$\frac{d}{dt} \begin{pmatrix} \rho_1^S \\ \rho_2^{S,*} \\ \rho_3^{S,*} \\ \rho_4^S \\ \rho_5^G \\ \rho_6^S \\ \rho_7^G \end{pmatrix} = \begin{bmatrix} -(k_{1,1} + k_{1,2}) & 0 & 0 & 0 & 0 \\ k_{1,1} & -k_{2,1} & 0 & 0 & 0 \\ k_{1,2} & 0 & -k_{3,1} & 0 & 0 \\ 0 & \gamma_{2,1,4}k_{2,1} & 0 & 0 & 0 \\ 0 & \gamma_{2,1,5}k_{2,1} & 0 & 0 & 0 \\ 0 & 0 & \gamma_{3,1,6}k_{3,1} & 0 & 0 \\ 0 & 0 & \gamma_{3,1,7}k_{3,1} & 0 & 0 \end{bmatrix} \cdot \begin{pmatrix} \rho_1^S \\ \rho_2^{S,*} \\ \rho_3^{S,*} \\ \rho_4^S \\ \rho_5^G \\ \rho_6^S \\ \rho_7^G \end{pmatrix} \quad (22)$$

This system of equations can be reduced removing dependent variables such that matrix \mathbf{A} is full rank. In addition, the mass conservation constraint $\gamma_{i,j,l+1} = (1 - \gamma_{i,j,l})$ allows to remove the two unknown mass coefficients for the pyrolysis gases. In total, considering the four reaction rates $k_{i,j}$, each of them having two free parameters, the four mass coefficients and the two consistency relations, the total number of parameters to be calibrated is thus equal to 10.

6. Results

In the following, the parameter optimization results based on the aforementioned kinetic model using the deterministic and Bayesian approaches are presented. Then, the result of this newly calibrated model is compared with current models from literature. Finally, the extrapolation capabilities of our calibrated model are explored by propagating and comparing with experimental results from the literature carried out at other heating rates.

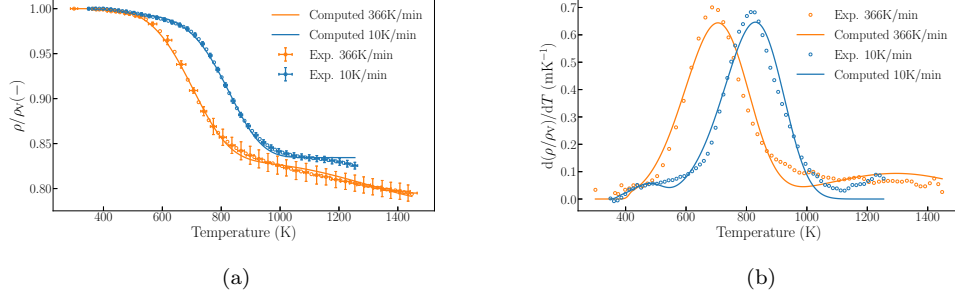


Figure 5: Comparison between the experiments and the calibrated model for the two different heating rate scenarios. On the left (a) are the curves for the normalized sample density and on the right (b) the normalized production rate curves as a function of temperature.

6.1. Deterministic approach

Fig. 5 shows that the calibrated model captures the behavior of the experimental data. Both the final state and its evolution are well reproduced by the proposed model. The shift in the production peak (Fig. 5b) towards lower temperatures with increasing heating rate is also well captured. This is in contrast with kinetic mechanisms based solely on parallel reactions that cannot achieve this match as it will be shown later.

The Arrhenius parameters for the calibrated model are summarized in Table 1. Consistently with the proposed model (Sect. 5), the activation energy $\mathcal{E}_{1,1}$ is lower than $\mathcal{E}_{1,2}$ (Table 1), indicating that the conversion towards $\rho_2^{S,*}$ starts earlier than the conversion towards $\rho_3^{S,*}$. The pre-exponential factor $\mathcal{A}_{1,1}$ is lower than $\mathcal{A}_{1,2}$ which indicates that the production of $\rho_2^{S,*}$ is slower than that of $\rho_3^{S,*}$. In summary, the calibrated kinetic parameters are all coherent with the underlying hypotheses of the model.

The production and the consumption of the different density variables

| Parameter | Value | Parameter | Value |
|--------------------------------|--------|---------------------|------------|
| $\log_{10}(\mathcal{A}_{1,1})$ | 2.019 | $\mathcal{E}_{1,1}$ | 32618.482 |
| $\log_{10}(\mathcal{A}_{1,2})$ | 14.292 | $\mathcal{E}_{1,2}$ | 143273.910 |
| $\log_{10}(\mathcal{A}_{2,1})$ | 0.442 | $\mathcal{E}_{2,1}$ | 51783.980 |
| $\log_{10}(\mathcal{A}_{3,1})$ | 0.993 | $\mathcal{E}_{3,1}$ | 31087.851 |
| $\gamma_{2,1,5}$ | 0.163 | $\gamma_{3,1,7}$ | 0.244 |

Table 1: Values for the calibrated parameters obtained from the deterministic optimization.

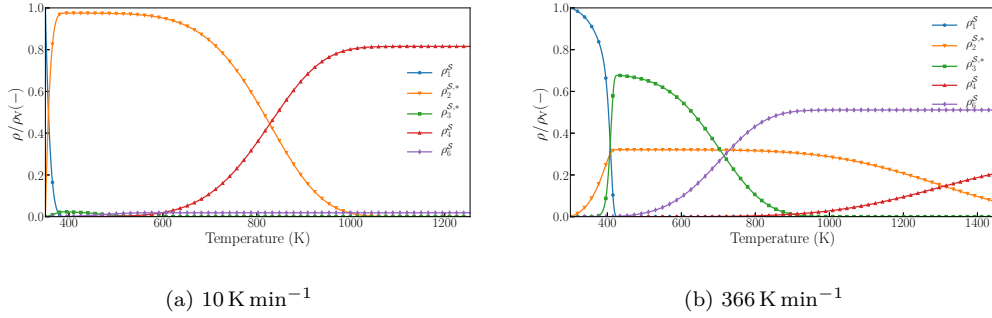


Figure 6: Evolution of the different solid densities for the calibrated model. It can be observed how the dominant pathway changes as the heating rate increases.

can also be observed from the plots presented in Fig. 6. At low heating rate (Fig. 6a), the initial solid is mostly converted into $\rho_2^{S,*}$, while the opposite occurs at high heating rates (Fig. 6b). These intermediate steps further react at higher temperatures generating the char yield.

6.2. Bayesian inference

The Markov chain is initiated using the results from the deterministic optimization shown Table 1. Owing to the relatively short burn-in enabled by using the previous optimization result, we run the chain for 10^4 iterations.

Fig. 7 presents the simulated data obtained from the inference compared

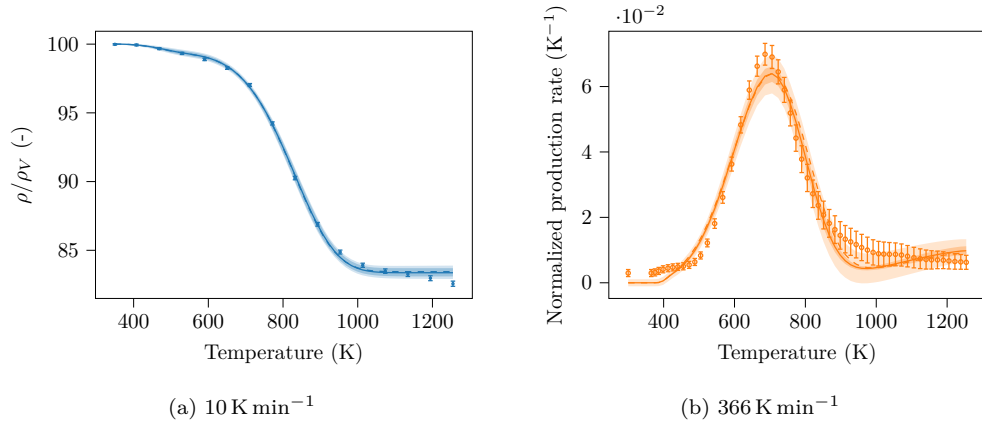


Figure 7: Mass loss curve at heating rate of 10 K min^{-1} (a) and production rate curve at heating rate 366 K min^{-1} (b) obtained with the uncertain parameters. The continuous lines are the computed mean at each temperature. The dashed lines are the initial calibrated model (maximum likelihood estimator). The shaded areas represent the credible interval (inner-darker shaded area) and the prediction interval (outer-lighter shaded area) respectively.

to the observed data to assess the validity of the model. We represented the mean value (solid line) and the credible and prediction intervals with bounds at 95% confidence (darker and lighter shadows, respectively). The credible interval takes only the parameter uncertainties obtained from the Bayesian inference. It does not take into account experimental uncertainties. By contrast, the prediction interval considers the experimental errors, and almost all the experimental data lie within the prediction interval as seen on Fig. 7. The model features an overall good agreement with the experimental data but some discrepancies as in Fig. 5 are again observed at high temperatures for 10 K min^{-1} and at low temperatures for 366 K min^{-1} . These discrepancies are not captured by the uncertainties on the parameters and this suggests that further complexities could be captured by improving models that will help reducing the overall model error. The negative value for some of the interval bounds at the onset and tail of the decomposition curves are due to the choice of the Gaussian additive noise for the error model from Eq. 10 over the whole temperature interval. Even though this does not occur in actual experiments.

Second, in Table 2, the values obtained for the mean, standard deviation and coefficient of variation (CV) are summarized for the marginal distributions directly estimated from the Markov chains. The mean values may be different from the previous deterministic values used to initiate the Markov chains. The mean value for $\gamma_{2,1,5}$ is very close to its deterministic value because this parameter is found to be the less correlated with all the other ones, as seen in the following. The CV provides a measure of the relative dispersion of the plausible parameter values with respect to the mean. The higher values

| Parameter | Mean | Std | CV | Parameter | Mean | Std | CV |
|--------------------------------|---------|--------|----------|---------------------|-----------|---------|---------|
| $\log_{10}(\mathcal{A}_{1,1})$ | 2.4768 | 0.3027 | 0.0.1222 | $\mathcal{E}_{1,1}$ | 26811.37 | 893.61 | 0.0333 |
| $\log_{10}(\mathcal{A}_{1,2})$ | 23.4935 | 1.1618 | 0.0494 | $\mathcal{E}_{1,2}$ | 183938.42 | 2369.64 | 0.0129 |
| $\log_{10}(\mathcal{A}_{2,1})$ | 0.2219 | 0.1238 | 0.5579 | $\mathcal{E}_{2,1}$ | 48796.41 | 1723.16 | 0.03531 |
| $\log_{10}(\mathcal{A}_{3,1})$ | 1.1969 | 0.0821 | 0.0686 | $\mathcal{E}_{3,1}$ | 33566.43 | 976.07 | 0.0291 |
| $\gamma_{2,1,5}$ | 0.1648 | 0.0038 | 0.0234 | $\gamma_{3,1,7}$ | 0.3190 | 0.0703 | 0.2202 |

Table 2: Values for the mean, standard deviation (std) and coefficient of variation (CV) for the calibrated parameters obtained from the Bayesian inference.

of the CVs for the reaction branch (2,1) for both $\mathcal{A}_{2,1}$ and $\mathcal{E}_{2,1}$ suggest that these two parameters are more difficult to identify and are more uncertain, although this reaction produces the component ρ_4^S at the two heating rates (Fig. 6) and thus more information is provided from the experimental data. This higher uncertainty is attributed to the slower process of the reaction (2,1) characterized by the low value of $\mathcal{A}_{2,1}$.

A graphical representation of the full correlation matrix is provided in Fig. 9. The correlation matrix is obtained from the estimated covariance matrix normalized by the standard deviations of the random parameters, such that diagonal terms of the correlation matrix are equal to one and off-diagonal terms range between 1 and -1. We note that the Arrhenius parameters \mathcal{A} and \mathcal{E} for the equations (2,1) and (3,1) are found to be highly correlated with a value for the correlation coefficient that is close to 1. This results in a wide range of values for the pre-exponential factor \mathcal{A} and the activation energy \mathcal{E} that can give satisfactory fits to the data. The high correlation is sometimes referred to as the kinetic compensation effect and has already been observed in past kinetics studies [31, 43, 44]. However, the pair of parameters

\mathcal{A} and \mathcal{E} for reaction (1,1) and (1,2) that are related to the production of the intermediate components are found to be less correlated. Besides the kinetic compensation effect for \mathcal{A} and \mathcal{E} , additional compensation mechanisms characterized by a high value for the correlation coefficient are observed: this is the case for example for the pair of parameters $\mathcal{A}_{1,1}$ with $\gamma_{3,1,7}$; $\mathcal{A}_{2,1}$ with $\gamma_{3,1,7}$; etc. There is only limited correlation with parameter $\gamma_{2,1,5}$ and results in the marginal distribution for which sampling has well converged (the closer to a Gaussian distribution). We finally note the high positive correlation value for the pair of parameters $\mathcal{A}_{1,1}$ with $\mathcal{A}_{1,2}$.

Finally, Fig. 8 represents the evolution of the densities as a function of the temperature (as in Fig. 6) but now with uncertainty intervals. It is observed in Fig. 8b that when both mechanisms are in competition, it is more uncertain to know what goes into which branch, leading to larger intervals and which also manifests itself in the high positive correlation between $\mathcal{A}_{1,1}$ with $\mathcal{A}_{1,2}$. This strong interaction between $\mathcal{A}_{1,1}$ with $\mathcal{A}_{1,2}$ is intrinsic to the competitive mechanisms: the uncertainties in these two parameters combine themselves and result in large uncertainty intervals in the densities when there is competition between the two reactions. On the other hand, for the pyrolysis at 10 K min^{-1} where the competition between the two reactions is less balanced, uncertainty ranges in the densities are tighter because the reaction is characterized mainly by the first branch of the mechanisms and is less influenced by the second one, as it can be corroborated on Fig. 8a.

The results of this section show that other parameter sets \mathbf{p}_0 can provide satisfactory results for representing the experimental results with their uncertainties. We were able to obtain samples from the posterior distribution using

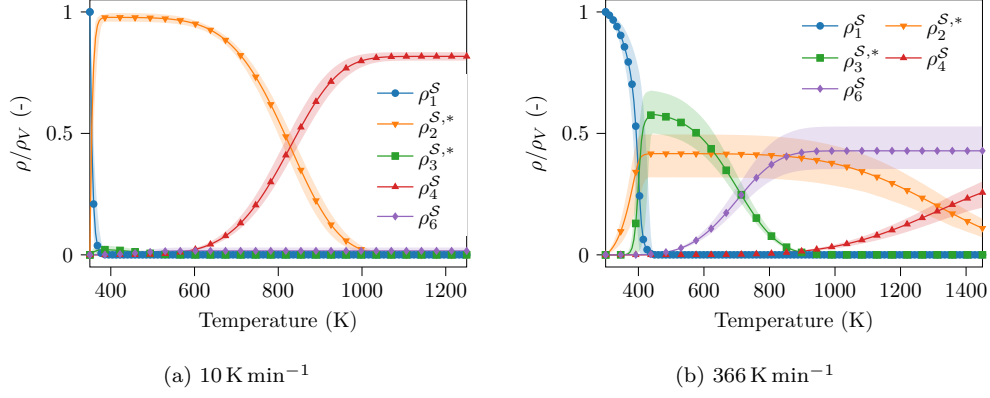


Figure 8: Evolution of the different solid densities for the calibrated model with their uncertainty intervals.

Markov chain and compare the model evaluations with the experimental data, thus taking into account the correlations between the input parameters. Not taking into account the correlation between the input parameters may lead to wrong results for the propagation and samples drawn directly from the Markov chain should be used for the uncertainty analysis. It was found that due to the nature of the competitive scheme and because a component can be both produced and consumed, there are additional kinetic compensation effects beyond the pair of parameters \mathcal{A} and \mathcal{E} , thus making the inference process even more uncertain.

6.3. Benchmark with other models

The proposed competitive model is compared to two other traditional devolatilization mechanisms [11, 12] for PICA, that feature parallel reactions schemes. First is the model of Lachaud et al. [11] developed for the Porous Material Analysis Toolbox (PATO) is based on a two-equation model built

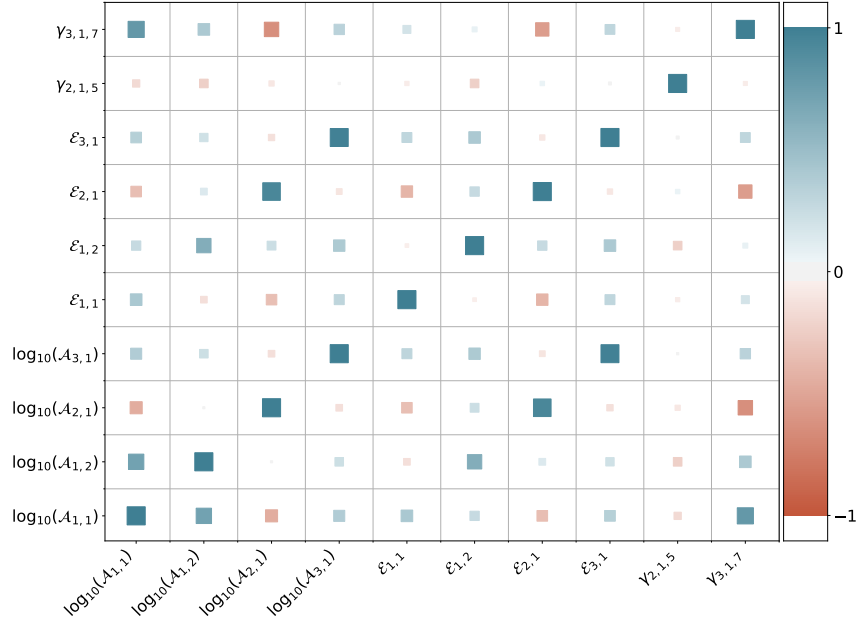


Figure 9: Graphical representation of the correlation matrix. The size of the squares is proportional to the magnitude of the elements of the matrix. On the colored graph, blue squares represent a positive correlation while red squares represent a negative correlation and the magnitude of the coefficient is represented on the side bar. The diagonal is characterized by the value of the correlation equal to 1 and off-diagonal terms vary between -1 (negative correlation) and 1 (positive correlation).

upon legacy data on the decomposition of phenolic [7–9]. Previous studies have shown that the model yields equivalent results to the baseline design model used in Fully Implicit Ablation and Thermal Analysis Program (FIAT) [10, 45]. Second is the model of Torres-Herrador et al. [12] that features a six reactions scheme and was calibrated on the pyrolysis experiment of Bessire and Minton at 366 K min^{-1} . The comparison is based on the same zero-dimensional chemical reactor simulations as used during the calibration

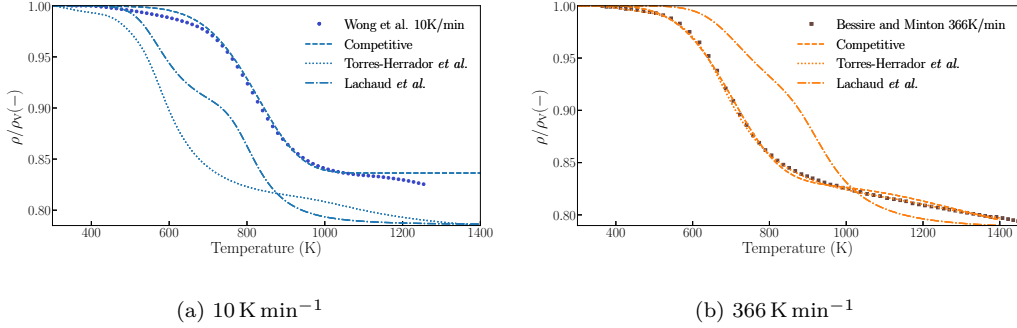


Figure 10: Comparison between proposed competitive model, the models of Lachaud [11] and of Torres-Herrador [12] and the experimental data.

step and is also the same used in [12].

As it can be seen in Fig. 10, the three models perform differently: the model calibrated from legacy data (Lachaud et al., [11]) does not agree with the new experimental measurements at either heating rates. The upgraded model of Torres-Herrador et al. ([12]) reproduces the degradation at the high heating rate for which it was calibrated (Fig. 10b), but fails to predict the behavior at low heating rate (Fig. 10a), under-predicting the pyrolysis temperature. In contrast, the competitive model can describe both low and high heating rates accurately.

This comparison shows that devolatilization mechanisms calibrated at a certain heating rate have limited applicability outside the calibration range and extrapolation can easily lead to largely erroneous predictions. In contrast, competitive models can include larger range of conditions, in addition to their capability to reproduce more complex behaviors. Very complex schemes can virtually be modeled, by adding bifurcation branches that become predominant as the heating rate changes.

6.4. Model behavior with temperature

The scarcity of thermal degradation data is one shortcoming often encountered when calibrating pyrolysis models. This is particularly true for specific resin systems such as the SC1008 phenolic of PICA for which comprehensive data that include quantification of pyrolysis products are only available at a limited number of conditions. Therefore, in this last section we finally test the performance of the developed competitive model at other heating rates than those used for the calibration in order to assess the prediction capabilities of the model to other conditions.

First, without any comparison to experimental results because of the lack of data in the literature, we look at how our model behaves when the heating rate progressively increased from 10 K min^{-1} up to 366 K min^{-1} , and in particular we look at how the production curve evolves. As seen on Fig. 11, when the heating rate increases from 10 K min^{-1} to 20 K min^{-1} , the expected shift towards higher pyrolysis temperatures is observed. This is because the process is still slow enough for the “slow branch” $k_{1,1}$ to be dominant in the process, converting most of the original reactant ρ_1^S to $\rho_2^{S,*}$. However, at a higher heating rate (50 K min^{-1}), $k_{1,2}$ starts to gain importance and the pyrolysis temperature starts shifting in the opposite direction reaching the other calibration heating rate (366 K min^{-1}). As the heating rate is increased even further (extrapolation of the kinetic scheme), the pyrolysis temperature shifts again towards higher temperatures.

Second, the proposed competitive model is compared to experimental results in order to assess the extrapolation capabilities of the model. Besides the 366 K min^{-1} used for the calibration, three other heating rates for the

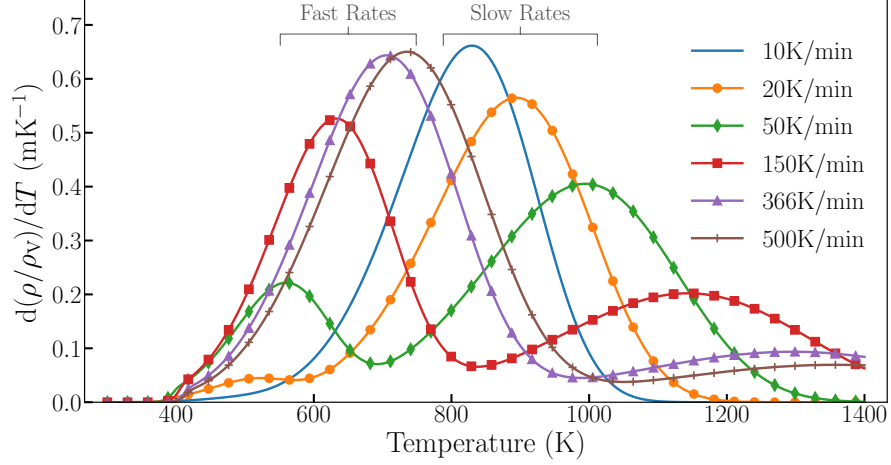


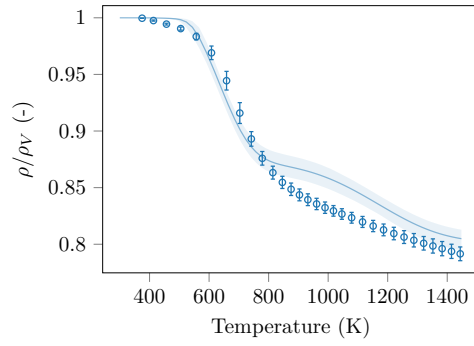
Figure 11: Model behavior at different heating rates. At 50 K min^{-1} , the fast reaction (corresponding to $k_{1,2}$ starts becoming dominant shifting the main decomposition peak towards lower temperatures.)

decomposition of PICA at 186 , 762 and 1500 K min^{-1} are available from the work of Bessire and Minton [19]. We take advantage of those additional experimental results that were not used to calibrate our model in order to compare and assess its validity when extrapolated to those heating rate. The comparison is presented in Fig. 12. The propagation of the uncertain parameters allow us to establish whether the observed discrepancies between the model and the experimental curves come from parameter uncertainties. For 186 K min^{-1} (Fig. 12a), it might be the case at low temperature and high temperature. However, there is a clear discrepancy between 800 K and 1300 K due to the model. The same behavior is observed at 762 K min^{-1} (Fig. 12c) where model discrepancy occurs between 600 and 900 K . At the highest heating rate (1500 K min^{-1} , Fig. 12d), it shows substantial discrepancies,

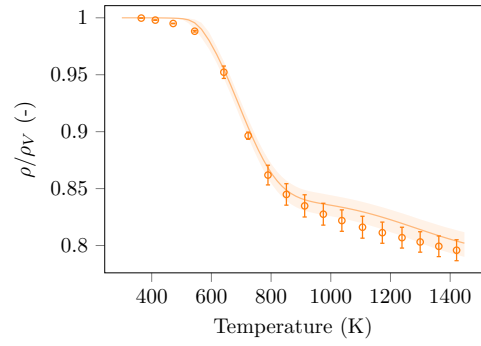
particularly below 800 K, and applying the current calibrated model to this heating rate is obviously wrong. These results emphasize that care must be taken when applying a pyrolysis model to other heating rates as unknown physical mechanisms may appear. Therefore, the model should be refined by adding more articulated branching evolutions of the present scheme in order to model these discrepancies and calibrate it with these curves. The new calibrated results would then look probably closer to the exact experimental results. Discrepancies could also come from other mechanisms than adding competitive reaction and we should for instance account for interactions between the gaseous products and the carbonaceous char, which are unaccounted for in the present model. We refer the reader to the experimental paper for a detailed discussion of the complexities that characterize the charring process of PICA [19]. Developing a dedicated finite rate kinetic model for the pyrolysis of PICA that fits the experimental results at all heating rates was beyond the scope of this study, but is the next necessary step towards the development of a comprehensive predictive material response model.

7. Conclusion

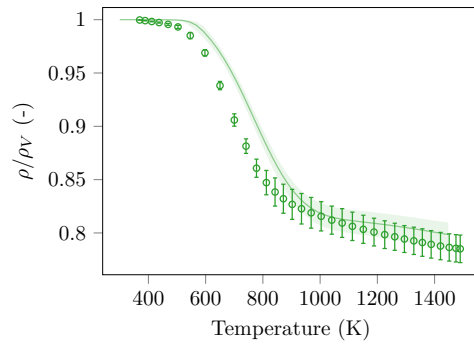
Experimental data from literature of pyrolysis of carbon/phenolic ablators showed behavior that could not be explained by the current devolatilization models. Therefore, we have studied the possibility of importing the competitive schemes typically used in biomass pyrolysis for aerospace heat shield materials.



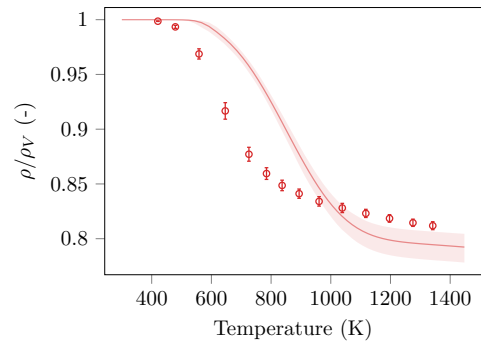
(a) 186 K min⁻¹



(b) 366 K min⁻¹



(c) 762 K min⁻¹



(d) 1500 K min⁻¹

Figure 12: Comparison with the different heating rates of Bessire and Minton [19].

A competitive kinetic mechanism coherent with the experimental measurements has been proposed and calibrated using first a deterministic and then a Bayesian optimization framework. Both optimization methods provide similar results, but the Bayesian method provides extra knowledge regarding the sensitivity of the competitive mechanism to the different kinetic parameters. The calibrated model closely follows the experimental measurements by Wong et al. [18] and by Bessire and Minton [19] at two distinct heating rate conditions.

The Bayesian analysis showed that there were several plausible values for the calibrated parameters and they were shown to be robust to the experimental data. However, some discrepancies are still observed between the physical model and the experiments and it is due to the choice of the physical model that might not be perfect. It was observed that the Markov chains for several parameters were slow to converge, even for the relatively simple model with few parameters considered here. Larger uncertainty intervals are observed when the two competitive branches are active during the reaction process and additional interaction effects between parameters. The high complexity of the parameter correlations, possible non-Gaussian posterior distribution and large dimensions suggest to investigate in the future more sophisticated algorithms that adapt the covariance matrix of the proposal distribution to the posterior distribution for a more efficient parameter inference.

Finally, we have shown the limitation of devolatilization models to predict the degradation of carbon/phenolic at different heating rates and how competitive mechanisms can cope with this limitation.

Acknowledgments

The research of F. Torres Herrador is supported by SB PhD fellowship 1S58718N of the Research Foundation Flanders (FWO). The second author work is supported by the Fund for Research Training in Industry and Agriculture (FRIA) provided by the Belgian Fund for Scientific Research (F.R.S.-FNRS). F. Panerai work is supported by NASA grant 80NSSC19M0164. The overall research is effort is supported by the NASA Entry System Modeling Project.

We would like to acknowledge Dr. Bessire for the useful discussions.

Developers of Spotpy are acknowledged for their support with the optimization software.

References

- [1] F. Panerai, J. C. Ferguson, J. Lachaud, A. Martin, M. J. Gasch, N. N. Mansour, Micro-tomography based analysis of thermal conductivity, diffusivity and oxidation behavior of rigid and flexible fibrous insulators, *International Journal of Heat and Mass Transfer* 108 (2017) 801–811. doi:10/f95p4d.
- [2] J. C. Ferguson, F. Panerai, J. Lachaud, N. N. Mansour, Theoretical study on the micro-scale oxidation of resin-infused carbon ablators, *Carbon* 121 (2017) 552–562. doi:10/gbptt2.
- [3] C. Szalai, E. Slimko, P. Hoffman, Mars Science Laboratory Heatshield Development, Implementation, and Lessons Learned, in: *Journal of Spacecraft and Rockets*, Vol. 51, 2014, pp. 1167–1173. doi:10/f6ftx5.

- [4] D. Kontinos, M. Stackpoole, Post-Flight Analysis of the Stardust Sample Return Capsule Earth Entry, in: 46th AIAA Aerospace Sciences Meeting and Exhibit, American Institute of Aeronautics and Astronautics, Reno, Nevada, 2008. doi:10.2514/6.2008-1197.
- [5] J. B. Scoggins, J. Rabinovitch, B. Barros-Fernandez, A. Martin, J. Lachaud, R. L. Jaffe, N. N. Mansour, G. Blanquart, T. E. Magin, Thermodynamic properties of carbon-phenolic gas mixtures, *Aerospace Science and Technology* 66 (2017) 177–192. doi:10/gd8dh9.
- [6] A. Bennett, D. R. Payne, R. W. Court, Pyrolytic and Elemental Analysis of Decomposition Products from a Phenolic Resin, *Macromolecular Symposia* 339 (1) (2014) 38–47. doi:10/f2rt6s.
- [7] G. F. Sykes, Decomposition Characteristics of a Char-Forming Phenolic Polymer Used for Ablative Composites., Tech. Rep. TN D-3810 (1967).
- [8] H. E. Goldstein, Pyrolysis Kinetics of Nylon 6–6, Phenolic Resin, and Their Composites, *Journal of Macromolecular Science: Part A - Chemistry* 3 (4) (1969) 649–673. doi:10.1080/10601326908053834.
- [9] K. A. Trick, T. E. Saliba, S. S. Sandhu, A kinetic model of the pyrolysis of phenolic resin in a carbon/phenolic composite, *Carbon* 35 (3) (1997) 393–401. doi:10.1016/S0008-6223(97)89610-8.
- [10] F. Milos, Y.-K. Chen, Comprehensive model for multicomponent ablation thermochemistry, 35th Aerospace Sciences Meeting and Exhibit (Jan. 1997). doi:10/gc3g3z.

- [11] J. Lachaud, J. B. Scoggins, T. E. Magin, M. G. Meyer, N. N. Mansour, A generic local thermal equilibrium model for porous reactive materials submitted to high temperatures, *International Journal of Heat and Mass Transfer* 108, Part B (2017) 1406–1417. doi:10.1016/j.ijheatmasstransfer.2016.11.067.
- [12] F. Torres-Herrador, J. B. E. Meurisse, F. Panerai, J. Blondeau, J. Lachaud, B. K. Bessire, T. E. Magin, N. N. Mansour, A high heating rate pyrolysis model for the Phenolic Impregnated Carbon Ablator (PICA) based on mass spectroscopy experiments, *Journal of Analytical and Applied Pyrolysis* (May 2019). doi:10/gf27n7.
- [13] P. Tadini, N. Grange, K. Chetehouna, N. Gascoin, S. Senave, I. Reynaud, Thermal degradation analysis of innovative PEKK-based carbon composites for high-temperature aeronautical components, *Aerospace Science and Technology* 65 (2017) 106–116. doi:10/f94vtf.
- [14] M. Rivier, J. Lachaud, P. M. Congedo, Ablative thermal protection system under uncertainties including pyrolysis gas composition, *Aerospace Science and Technology* 84 (2019) 1059–1069. doi:10/ggd9mz.
- [15] J. B. E. Meurisse, J. Lachaud, F. Panerai, C. Tang, N. N. Mansour, Multidimensional material response simulations of a full-scale tiled ablative heatshield, *Aerospace Science and Technology* 76 (2018) 497–511. doi:10/gc4pgh.
- [16] W. M. Jackson, R. T. Conley, High temperature oxidative degradation

- of phenol–formaldehyde polycondensates, *Journal of Applied Polymer Science* 8 (5) (1964) 2163–2193. doi:10/cbfhmp.
- [17] E. H. Stokes, Kinetics of pyrolysis mass loss from cured phenolic resin, *Journal of Thermophysics and Heat Transfer* 9 (2) (1995) 352–358. doi:10.2514/3.667.
- [18] H.-W. Wong, J. Peck, J. Assif, F. Panerai, J. Lachaud, N. N. Mansour, Detailed analysis of species production from the pyrolysis of the Phenolic Impregnated Carbon Ablator, *Journal of Analytical and Applied Pyrolysis* 122 (2016) 258–267. doi:10/f9h46d.
- [19] B. K. Bessire, T. K. Minton, Decomposition of Phenolic Impregnated Carbon Ablator (PICA) as a Function of Temperature and Heating Rate, *ACS Applied Materials & Interfaces* 9 (25) (2017) 21422–21437. doi:10.1021/acsami.7b03919.
- [20] J. Blondeau, H. Jeanmart, Biomass pyrolysis at high temperatures: Prediction of gaseous species yields from an anisotropic particle, *Biomass and Bioenergy* 41 (2012) 107–121. doi:10/f3zmcx.
- [21] R. S. Miller, J. Bellan, A Generalized Biomass Pyrolysis Model Based on Superimposed Cellulose, Hemicellulose and Lignin Kinetics, *Combustion Science and Technology* 126 (1-6) (1997) 97–137. doi:10.1080/00102209708935670.
- [22] C. Di Blasi, Modeling chemical and physical processes of wood and biomass pyrolysis, *Progress in Energy and Combustion Science* 34 (1) (2008) 47–90. doi:10/cszkrc.

- [23] E. Ranzi, A. Cuoci, T. Faravelli, A. Frassoldati, G. Migliavacca, S. Pierucci, S. Sommariva, Chemical Kinetics of Biomass Pyrolysis, *Energy & Fuels* 22 (6) (2008) 4292–4300. doi:10.1021/ef800551t.
- [24] J. Blondeau, Investigation of pulverised biomass combustion: detailed modelling of particle pyrolysis and experimental analysis of ash deposition, Ph.D. thesis, Université catholique de Louvain (May 2013).
- [25] F. Torres-Herrador, J. Coheur, J. Blondeau, J. Meurisse, F. Panerai, J. Lachaud, T. Magin, N. N. Mansour, Comparison between traditional and competitive reaction models for the pyrolysis of high temperature aerospace materials, in: *AIAA Aviation 2019 Forum*, American Institute of Aeronautics and Astronautics, 2019. doi:10.2514/6.2019-3361.
- [26] C. Lautenberger, A. C. Fernandez-Pello, Optimization Algorithms for Material Pyrolysis Property Estimation, *Fire Safety Science* 10 (2011) 751–764.
- [27] S. H. Cheung, K. Miki, E. Prudencio, C. Simmons, Uncertainty quantification and robust predictive system analysis for high temperature kinetics of HCN/O₂/ar mixture, *Chemical Physics* 475 (2016) 136–152. doi:10.1016/j.chemphys.2016.05.026.
- [28] N. Galagali, Y. M. Marzouk, Bayesian inference of chemical kinetic models from proposed reactions, *Chemical Engineering Science* 123 (2015) 170–190. doi:10.1016/j.ces.2014.10.030.
- [29] H. Najm, R. Berry, C. Safta, K. Sargsyan, B. Debusschere, Data-free inference of uncertain parameters in chemical models, *International*

- Journal for Uncertainty Quantification 4 (2014) 111–132. doi:10.1615/Int.J.UncertaintyQuantification.2013005679.
- [30] J. Urzay, N. Kseib, P. G. Constantine, D. F. Davidson, G. Iaccarino, Uncertainty-quantifying models for chemical-kinetic rates, Center for Turbulence Research Annual Briefs (2012).
 - [31] M. C. Bruns, Inferring and propagating kinetic parameter uncertainty for condensed phase burning models, Fire Technology 52 (1) (2015) 93–120. doi:10.1007/s10694-015-0457-2.
 - [32] M. C. Kennedy, A. O’Hagan, Bayesian calibration of computer models, Journal of the Royal Statistical Society: Series B (Statistical Methodology) 63 (3) (2001) 425–464. doi:10.1111/1467-9868.00294.
 - [33] R. C. Smith, Uncertainty Quantification: Theory, Implementation, and Applications, Society for Industrial and Applied Mathematics, Philadelphia, 2014.
 - [34] T. Houska, P. Kraft, A. Chamorro-Chavez, L. Breuer, SPOTting Model Parameters Using a Ready-Made Python Package, PLOS ONE 10 (12) (2015) e0145180. doi:10/gf27q5.
 - [35] Q. Y. Duan, V. K. Gupta, S. Sorooshian, Shuffled complex evolution approach for effective and efficient global minimization, Journal of Optimization Theory and Applications 76 (3) (1993) 501–521. doi:10/DTF26t.
 - [36] C. P. Robert, G. Casella, Monte Carlo Statistical Methods, Springer N.-Y., 1999. doi:10.1007/978-1-4757-3071-5.

- [37] N. Metropolis, A. W. Rosenbluth, M. N. Rosenbluth, A. H. Teller, E. Teller, Equation of state calculations by fast computing machines, *The Journal of Chemical Physics* 21 (6) (1953) 1087–1092. doi:10.1063/1.1699114.
- [38] W. K. Hastings, Monte Carlo sampling methods using Markov chains and their applications, *Biometrika* 57 (1) (1970) 97–109. doi:10.1093/biomet/57.1.97.
- [39] W. R. Gilks, S. Richardson, D. J. Spiegelhalter, *Markov Chain Monte Carlo in Practice*, Chapman & Hall/CRC, London, 1996.
- [40] L. Torre, J. M. Kenny, A. M. Maffezzoli, Degradation behaviour of a composite material for thermal protection systems Part I Experimental characterization, *Journal of Materials Science* 33 (12) (1998) 3137–3143. doi:10.1023/A:1004399923891.
- [41] H.-W. Wong, J. Peck, R. E. Bonomi, J. Assif, F. Panerai, G. Reinisch, J. Lachaud, N. N. Mansour, Quantitative determination of species production from phenol-formaldehyde resin pyrolysis, *Polymer Degradation and Stability* 112 (2015) 122–131. doi:10.1016/j.polymdegradstab.2014.12.020.
- [42] W. H. Press, S. A. Teukolsky, Savitzky-Golay smoothing filters, *Computers in Physics* 4 (6) (1990) 669–672. doi:10/gf3m8t.
- [43] N. Koga, A review of the mutual dependence of Arrhenius parameters evaluated by the thermoanalytical study of solid-state reactions: the

kinetic compensation effect, *Thermochimica Acta* 244 (1994) 1–20. doi:
10.1016/0040-6031(94)80202-5.

- [44] A. K. Galwey, M. E. Brown, *Thermal Decomposition of Ionic Solids*, Elsevier, Amsterdam, 1999.
- [45] A. D. Omidy, F. Panerai, A. Martin, J. Lachaud, I. Cozmuta, N. N. Mansour, Code-to-Code Comparison, and Material Response Modeling of Stardust and MSL using PATO and FIAT, Technical Report NASA/CR-2015-218960, NASA Ames Research Center (Jun. 2015).